Bulut, F., Bohnhoff, M., Eken, T., Janssen, C., Kilic, T., Dresen, G. (2012): The East Anatolian Fault Zone: Seismotectonic setting and spatiotemporal characteristics of seismicity based on precise earthquake locations. - Journal of Geophysical Research, 117, B07304, 10.1029/2011JB008966

The East Anatolian Fault Zone: Seismotectonic setting and spatiotemporal characteristics of seismicity based on precise earthquake locations

Fatih Bulut,[1] Marco Bohnhoff,[1] Tuna Eken,[1] Christoph Janssen,[1] Tuğbay Kılıç,[2] and Georg Dresen[1]

Received 25 October 2011; revised 13 April 2012; accepted 22 May 2012; published 17 July 2012.

[1] The East Anatolian Fault Zone (EAFZ) represents a plate boundary extending over ~500 km between the Arabian and Anatolian plates. Relative plate motion occurs with slip rates ranging from 6 to 10 mm/yr and has resulted in destructive earthquakes in eastern Turkey as documented by historical records. In this study, we investigate the seismic activity along the EAFZ and fault kinematics based on recordings from a densified regional seismic network providing the best possible azimuthal coverage for the target region. We optimize a reference 1-D velocity model using a grid-search approach and re-locate hypocenters using the Double-Difference earthquake relocation technique. The refined hypocenter catalog provides insights into the kinematics and internal deformation of the fault zone down to a resolution ranging typically between 100 and 200 m. The distribution of hypocenters suggests that the EAFZ is characterized by NE-SW and E-W oriented sub-segments that are sub-parallel to the overall trend of the fault zone. Faulting mechanisms are predominantly left-lateral strike-slip and thus in good correlation with the deformation pattern derived from regional GPS data. However, we also observe local clusters of thrust and normal faulting events, respectively. While normal faulting events typically occur on NS-trending subsidiary faults, thrust faulting is restricted to EW-trending structures. This observation is in good accordance with kinematic models proposed for evolving shear zones. The observed spatiotemporal evolution of hypocenters indicates a systematic migration of micro- and moderate-sized earthquakes from the main fault into adjacent fault segments within several days documenting progressive interaction between the major branch of the EAFZ and its secondary structures. Analyzing the pre versus post-seismic phase for M > 5 events we find that aftershock activities are initially spread to the entire source region for several months but start to cluster at the central part of the main shock rupture thereafter.

Citation: Bulut, F., M. Bohnhoff, T. Eken, C. Janssen, T. Kılıç, and G. Dresen (2012), The East Anatolian Fault Zone: Seismotectonic setting and spatiotemporal characteristics of seismicity based on precise earthquake locations, *J. Geophys. Res.*, *117*, B07304, doi:10.1029/2011JB008966.

1. Introduction

[2] The westward movement of the Anatolian plate has developed in the frame of the northward moving Arabian plate and the southward rollback of the Hellenic subduction zone where the African lithosphere is subducted below the Aegean plate (Figure 1). The East Anatolian Fault Zone (EAFZ hereafter) is one of the major elements in this tectonic framework representing a left-lateral strike-slip plate boundary extending over ~500 km between the Arabian and Anatolian plates in eastern Turkey. The continuing northward migration of the Arabian plate with respect to stable Eurasia since the Miocene resulted in the westward extrusion of the Anatolian plate along the North and East Anatolian Fault Zones, respectively (NAFZ and EAFZ Figure 1) [e.g., *McKenzie*, 1972, 1978; *Şengör*, 1979; *Dewey and Şengör*, 1979; *Şengör and Yilmaz*, 1981; *Şengör et al.*, 2005]. However, the Arabian Plate currently does not seem to play a major role in driving the westward motion of the Anatolian plate as determined from GPS measurements and the fault kinematics surrounding the Arabian plate (Figure 1b) [*Reilinger et al.*, 2006].

[3] The EAFZ was first described by *Allen* [1969] and mapped by *Arpat and Şaroğlu* [1972], however, its exact

[1]Helmholtz Centre Potsdam, GFZ German Research Centre for Geosciences, Potsdam, Germany.
[2]Disaster and Emergency Management Presidency, Ankara, Turkey.

Corresponding author: F. Bulut, Helmholtz Centre Potsdam, GFZ German Research Centre for Geosciences, Potsdam D-14473, Germany. (bulut@gfz-potsdam.de)

0148-0227/12/2011JB008966

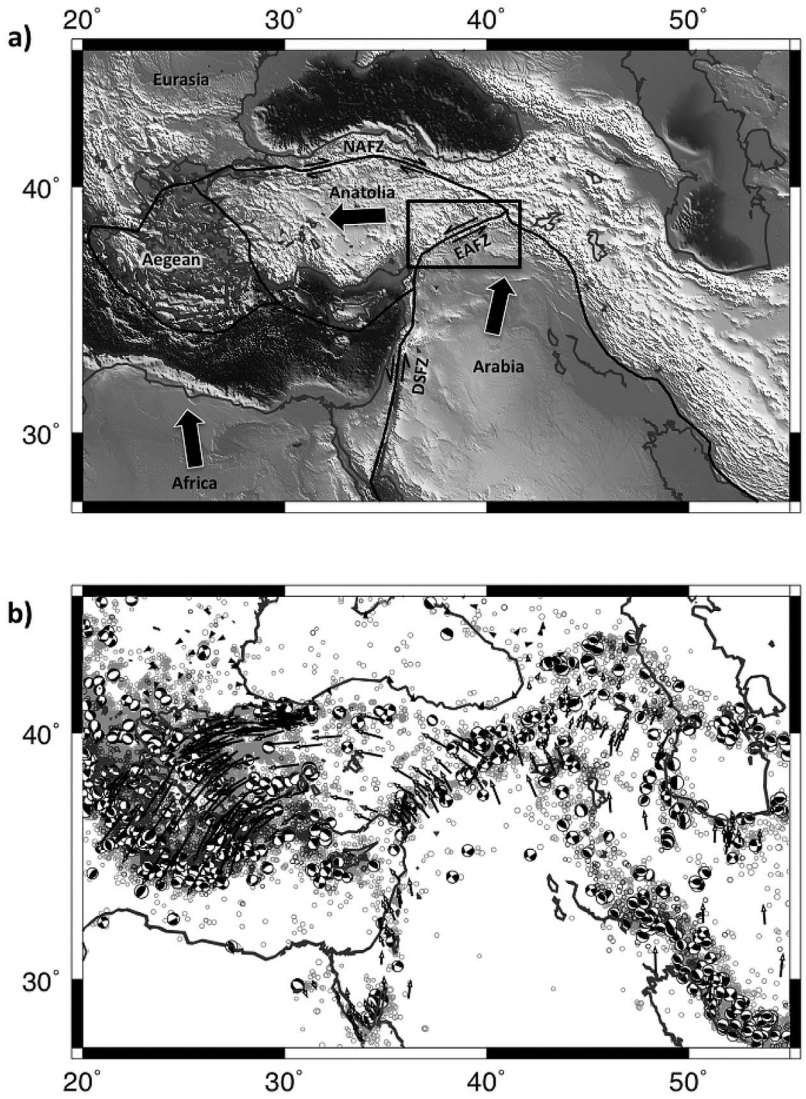

Figure 1. (a) Tectonic setting and topographic map of the greater Eastern Mediterranean – Anatolian – Northern Arabian region: This study focuses on the East Anatolian Fault Zone (EAFZ), which represents a geological boundary between the Arabian plate and westward moving Anatolian plate. Black lines represent major plate boundaries [after *Bird*, 2003]. Topographic data has been obtained from http://topex.ucsd.edu/WWW_html/srtm30_plus.html. The rectangle indicates the study area that is enlarged in Figure 2. Arrows are simplified plate motions with respect to stable Eurasia. (b) Present-day seismotectonics of the region. Fault plane solutions are extracted from Harvard CMT catalog. Circles indicate the earthquake locations for M > 4 events based on the U.S.G.S earthquake catalog since 1976 (http://earthquake.usgs.gov). Epicenters are color coded based on depth (gray: depth <40 km, black: depth >40 km). GPS vectors are obtained from *Reilinger et al.* [2006].

length is an embattled question. According to *Over et al.* [2004] and *Yilmaz et al.* [2006], the EAFZ extends from the Karliova triple junction where it joins the NAFZ toward the southwest for about 600 km to the Kahramanmaras triple junction near Antakya, where it joins the Dead Sea Fault Zone (DSFZ in Figure 1) [*Şengör et al.*, 1985; *Westaway*, 2004]. The EAFZ comprises several distinct strands with localized pull-apart basins and push-up zones rather than a throughgoing continuous fault plane [*Şengör et al.*, 1985; *Westaway*, 1994; *Emre and Duman*, 2007]. Based on fault geometry and strike of the strands, the EAFZ consists of five [*Hempton et al.*, 1981] or six segments [*Saroglu et al.*, 1992]. The age of the fault zone remains to be controversial, but it likely formed between Late Miocene-Early Pliocene [e.g., *Şengör et al.*, 1985; *Hempton*, 1987] to Late Pliocene [e.g., *Emre and Duman*, 2007].

[4] The current slip rate across the EAFZ varies between 6 and 10 mm/y following different measurement techniques (seismic moments of earthquakes [*Taymaz et al.*, 1991]; GPS measurements [*McClusky et al.*, 2000]). Left-lateral displacement along the EAFZ is also confirmed by seismological observations [*McKenzie*, 1972; *Taymaz et al.*, 1991; *Örgülü et al.*, 2003] and geological studies [*Saroglu et al.*, 1992]. However, there is a significant difference between

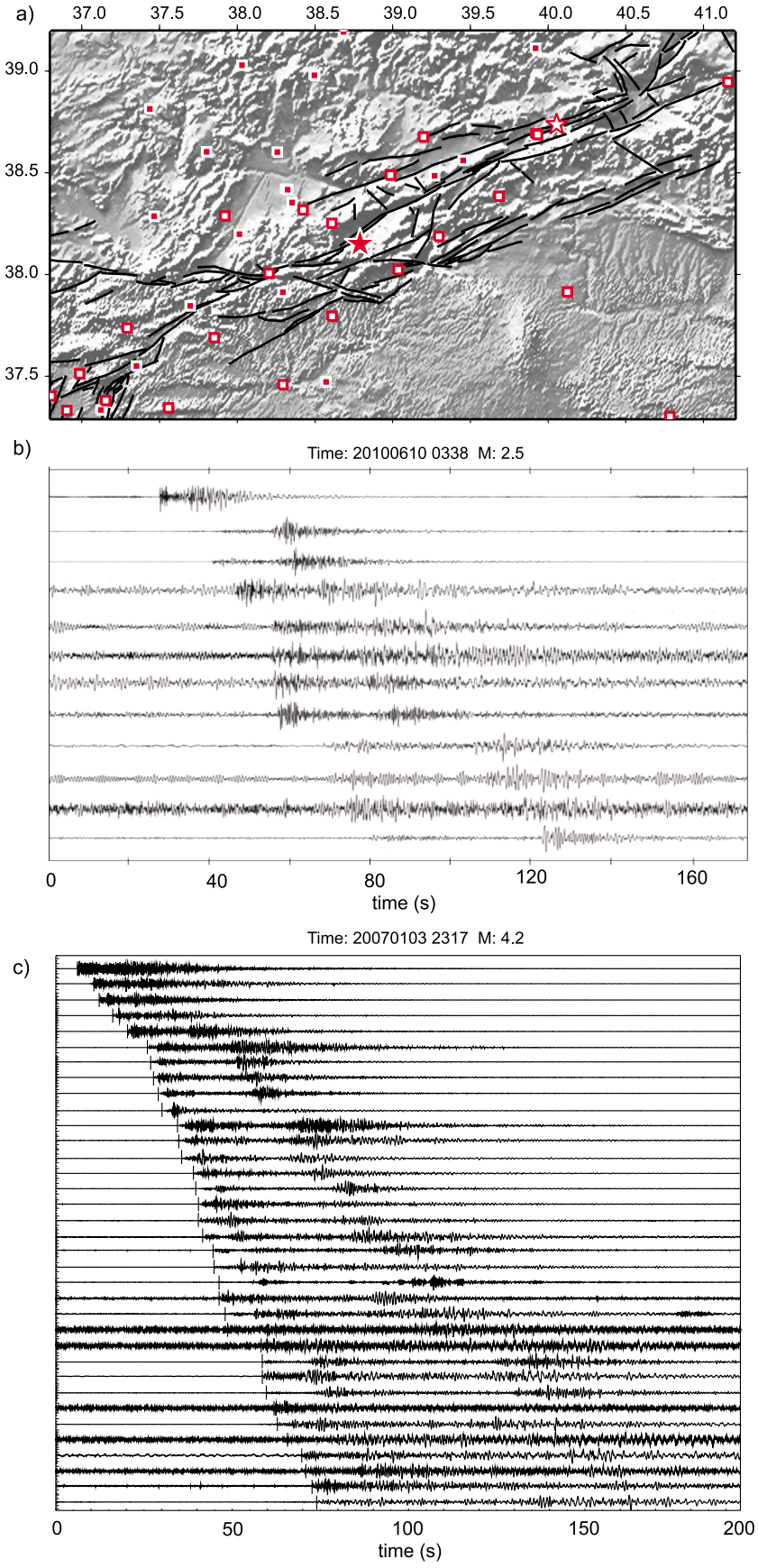
a)
37.0
37.5
38.0
38.5
39.0
39.5
40.0
40.5
41.0
39.0
38.5
38.0
37.5
b)
Time: 20100610 0338 M: 2.5
0
40
80
120
160
time (s)
Time: 20070103 2317 M: 4.2
c)
0
50
100
150
200
time (s)

Figure 2

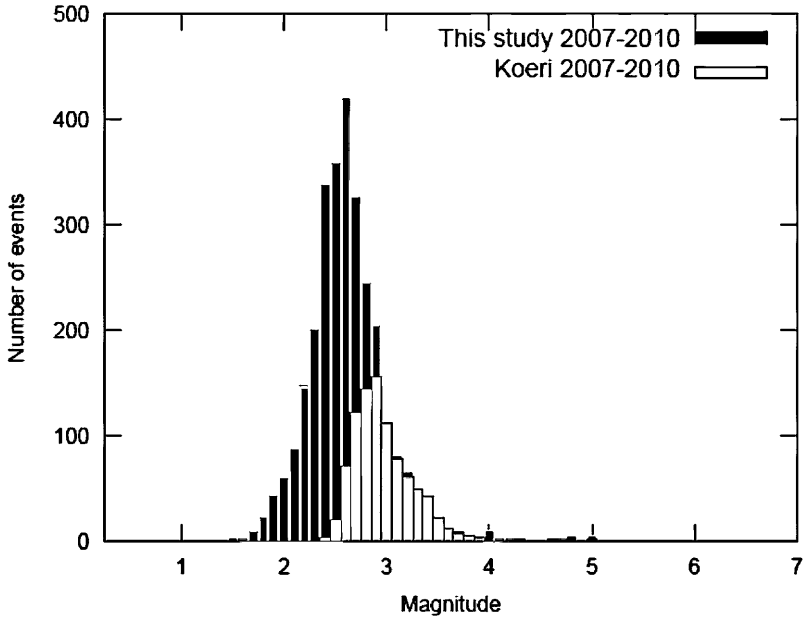

Figure 3. Magnitude-frequency distribution for the earthquake catalog obtained in this study (black bars) and for the KOERI earthquake catalog (white bars). The long-term magnitude of completeness (Mc) from the KOERI catalog is ~2.9 while Mc for the database of this study is ~2.6.

the estimates of the accumulated overall offset. An upper bound of 27–33 km is constrained by the offset of geological features and by the length of the Golbasi strike-slip basin [*Westaway and Arger*, 1996]. The lower bound (15–22 km) is based on offset drainage channels on individual fault segments [*Hempton*, 1987]. Sliding along the fault resulted in destructive M > 7 earthquakes in Eastern Turkey as reported in historical earthquake catalog [*Ambraseys*, 1971]. Interestingly, during the last century the EAFZ has produced only one large earthquake (M = 6.8) whereas the North Anatolian Fault Zone hosted a remarkable sequence of westward migrating M + 7 earthquakes that activated almost the entire NAFZ [e.g., *Toksöz et al.*, 1979]. Most likely this has been the other way around in the preceding several centuries, that is, the EAFZ was seismically active while the NAFZ was relatively silent [*Ambraseys*, 1971].

[5] Historical and instrumental records reveal significant differences between historical and recent seismicity, respectively. The largest known earthquakes along the EAFZ occurred on November 29, 1114 (M > 7.8), March 28, 1513 (M > 7.4) and March 2, 1893 (M > 7.1) [*Ambraseys and Jackson*, 1998], respectively. These large devastating historical earthquakes contrast with only one large earthquake during the last century (on December 4, 1905; M = 6.8) [*Nalbant et al.*, 2002]. *Çetin et al.* [2003] interpreted the apparent seismic quiescence along the entire EAFZ to indicate that the fault is currently locked.

[6] In this study, we present results from the analysis of seismic data recorded by a newly deployed seismic network covering the entire EAFZ. The primary objective of this study is to determine high-precision hypocenter locations in order to characterize space-time relations of seismicity along the fault system and to investigate the fault structure and its kinematics. This analysis provides insights into the seismotectonic settings along the entire EAFZ on a well-resolved scale for the first time. The results allow to better characterize the development of the EAFZ and its role in the regional kinematical frame.

2. Data Base and Analysis

2.1. Data Base

[7] The regional magnitude of completeness has been lowered by a seismic network deployed in 2007 along the entire EAFZ. This substantially enlarged the hypocenter database and thus allowed for an improved spatial sampling of the seismically active fault zone. We aim at investigating fault segmentation of the EAFZ as well as the interaction of sub-segments combining data from available regional seismic stations operated by (1) the Kandilli Observatory Earthquake Research Institute (KOERI) and (2) the Directorate of Disaster Affairs (AFAD) to achieve the best possible hypocenter locations. The combined network consists of 39 seismographs located in the vicinity of the EAFZ (see Figure 2a, open squares: AFAD stations, red squares: KOERI stations). Figures 2b and 2c shows a waveform example for two local earthquakes (M = 2.5 and M = 4.2, respectively). The upgraded network allowed lowering the regional

Figure 2. (a) Station distribution of the combined seismic network used to monitor seismicity throughout the EAFZ region. Squares represent the seismograph locations (white: stations operated by Directorate of Disaster Affairs 'AFAD', red: stations operated by Kandilli Observatory Earthquake Research Institute 'KOERI') and the black lines indicate mapped active faults (http://www.deprem.gov.tr). Topographic data has been obtained from http://topex.ucsd.edu/WWW_html/srtm30_plus.html. (b) Waveform example for a small (M = 2.5, epicenter shown by open star in Figure 2a) and (c) moderate size earthquake (M = 4.2, epicenter shown by red star in Figure 2a). Recordings are sorted by hypocentral distance.

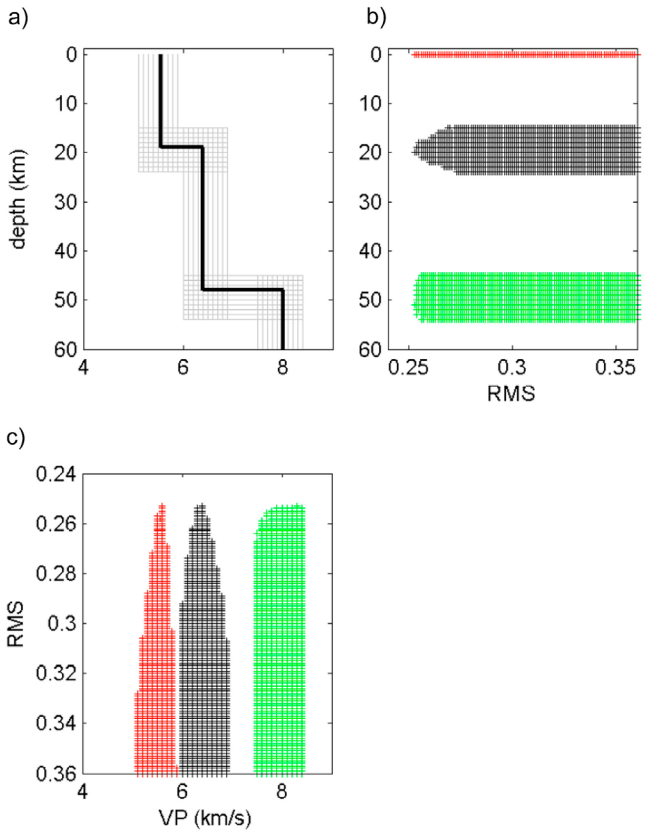

Figure 4. Optimization of the reference 1-D velocity model: (a) Grey lines represent the model space searched over and the black line is the final model determined based on data misfit (RMS). (b) Root mean square of the travel time misfits versus the depth of interface. (c) Root mean square of the travel time misfits versus the P wave velocity.

magnitude of completeness from M2.9 to M2.6 (Figure 3). The time period covered by our data set is 01/2007–08/2011. Furthermore, we extend the time period considered here (2007–2011) including the seismicity catalog provided by KOERI (2002–2007) in order to investigate the overall spatiotemporal distribution of seismicity along the entire EAFZ over a larger time period.

2.2. Data Analysis

[8] Continuous seismic recordings from the combined network are processed following a state of the art network processing procedure resulting in a total of 3751 located events. Events are detected using a STA/LTA (short-term average/long-term average) trigger. Event windows are extracted once the signal-to-noise ratio (SNR) simultaneously exceeds a given threshold at a minimum of six stations. Absolute hypocenter determination is performed using the HYPOCENTER earthquake location program [*Lienert and Havskov*, 1995]. For the travel time inversion, we use an optimized reference 1-D velocity model which we obtain using a grid-search approach. The earthquake subset used for velocity modeling is carefully selected to avoid instabilities in the inversion process that otherwise could be introduced by hypocenters with substantial uncertainties. The first iteration is performed to find an average P wave velocity in order to select well-constrained events. As we aim at minimizing uncertainties in hypocenter location caused by the velocity model we only use high-quality events for which the absolute location error is less than 2.0 km in both lateral and vertical direction, that have an RMS value smaller than 0.2 s, and that are recorded at a minimum of ten seismographs. S-wave readings are used to better constrain the earthquake locations fixing Vp/Vs = 1.73. We define a three-layered crustal model since the average spacing of stations is ~20 km. A grid search to find the optimal velocity-depth profile was performed locating the selected subset of events and iterating the

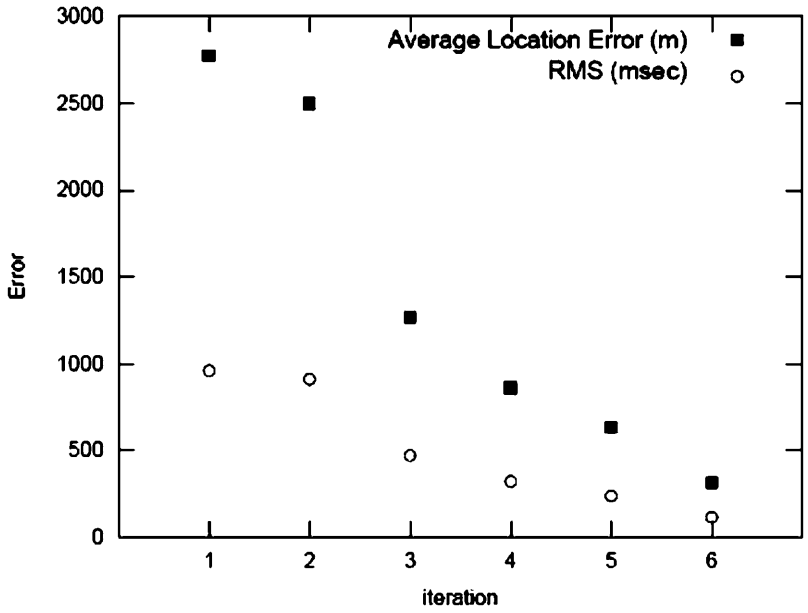

Figure 5. Iterative error reduction obtained using the double-difference relocation technique where errors refer to the average location error in m (black square) and the root-mean square in msec (white circles).

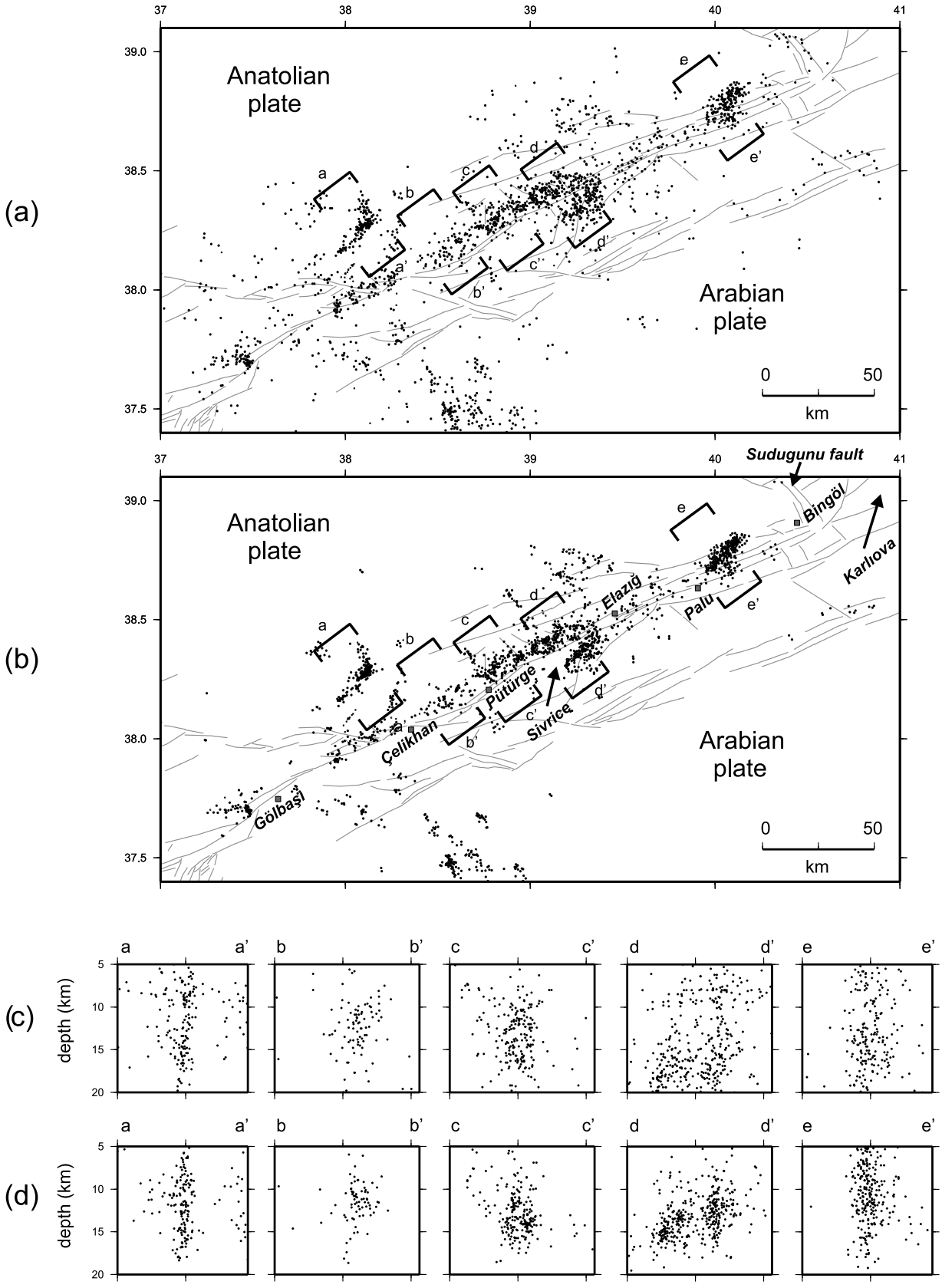

Figure 6. Epicentral map and depth sectional views for seismicity along the EAFZ obtained in this study based on (a, c) absolute locations and (b, d) double-difference derived relative locations, respectively. Black dots represent earthquake locations and the gray lines are presently active faults. Selected NW-SE trending transects indicated in Figures 6a and 6b and plotted as depth sections in Figures 6c and 6d.

Table 1. Focal Mechanisms

ID	Latitude (deg)	Longitude (deg)	Depth (km)	Strike (deg)	Dip (deg)	Rake (deg)	M	Year	m	d	h	Min	Source[a]	CC Coef
1	38.51	38.13	3	0	80	−90	5.5	1964	6	14	12	15	MCK	-
2	37.79	38.02	4	273	49	31	5.7	1986	5	5	3	35	TAY	-
3	37.91	38.01	10	275	27	30	5.5	1986	6	6	10	39	TAY	-
4	39.82	38.71	10	310	90	−180	5.0	1992	5	7	19	15	CMT	-
5	41.10	39.18	33	272	75	−175	4.8	1998	4	13	15	14	CMT	-
6	38.98	38.33	10	251	83	−7	4.9	1998	5	9	15	38	CMT	-
7	39.32	38.43	19	220	85	−10	3.6	1999	11	25	14	9	ORG	-
8	39.85	38.65	27	110	40	110	3.5	1999	12	14	3	20	ORG	-
9	38.95	38.30	13	345	72	−147	4.4	2000	1	2	20	28	ORG	-
10	39.81	38.65	5	324	79	164	4.4	2000	1	12	2	47	ORG	-
11	40.04	38.78	22	40	75	−10	3.6	2000	3	12	12	48	ORG	-
12	40.05	38.77	21	40	65	20	3.6	2000	3	12	13	45	ORG	-
13	40.05	38.78	17	40	90	0	3.5	2000	3	14	9	6	ORG	-
14	37.08	37.61	13	44	80	38	4.6	2000	4	2	11	41	ORG	-
15	37.32	37.54	10	224	89	−15	4.5	2000	4	2	17	26	ORG	-
16	39.69	38.59	27	271	58	42	3.3	2000	4	18	8	8	ORG	-
17	40.88	38.57	5	140	65	−150	3.5	2000	4	28	22	14	ORG	-
18	38.83	38.26	23	53	82	16	4.4	2000	5	7	9	8	ORG	-
19	39.21	38.41	7	245	83	−4	5.3	2004	8	11	15	48	CMT	-
20	38.91	38.27	22	320	87	167	4.5	2000	5	7	23	10	ORG	-
21	39.80	38.65	8	80	90	0	3.5	2000	6	29	19	7	ORG	-
22	39.50	38.54	2	160	80	170	3.4	2000	7	14	15	43	ORG	-
23	39.84	38.67	10	150	55	140	3.4	2000	7	28	19	22	ORG	-
24	38.43	38.02	10	338	74	−177	6.0	2002	11	19	1	25	INGV	-
25	40.53	39.04	10	333	67	−171	6.4	2003	5	1	0	27	CMT	-
26	39.00	38.32	10	72	89	1	5.4	2003	7	13	1	48	CMT	-
27	38.19	37.96	38	334	44	155	6.0	2004	2	26	4	14	INGV	-
28	39.60	38.61	10	116	43	95	6.0	2004	6	12	13	37	INGV	-
29	39.22	38.42	5	54	27	−106	6.0	2004	8	14	0	20	INGV	-
30	39.26	38.46	16	50	35	−104	6.0	2004	8	14	20	42	INGV	-
31	38.81	38.26	8	237	51	−20	5.3	2005	11	26	15	56	CMT	-
32	40.06	38.77	6	333	73	−172	4.6	2007	1	26	8	20	CMT	-
33	39.06	38.39	22	345	84	−177	5.0	2007	2	9	2	22	BUL	0.53
34	39.30	38.40	20	344	82	−166	5.9	2007	2	21	11	5	BUL	0.63
35	39.26	38.28	16	265	56	4	5.2	2007	2	28	19	55	BUL	0.51
36	39.22	38.29	10	160	85	135	4.0	2007	2	28	20	8	BUL	0.53
37	39.25	38.34	16	249	64	−5	4.3	2007	2	28	23	27	BUL	0.54
38	39.26	38.31	4	246	55	27	4.0	2007	2	28	23	28	BUL	0.56
39	40.46	39.04	6	149	69	168	4.8	2007	3	8	12	35	BUL	0.64
40	40.47	39.06	6	14	75	132	4.8	2007	3	9	11	24	BUL	0.54
41	39.28	38.35	4	262	47	3	4.5	2007	4	14	4	30	BUL	0.59
42	39.19	38.30	8	75	89	−28	4.2	2007	4	19	7	16	BUL	0.58
43	37.46	38.16	17	337	79	−175	4.4	2007	8	24	2	53	BUL	0.62
44	41.09	39.25	19	95	28	29	5.5	2007	8	25	10	5	BUL	0.58
45	36.93	37.82	14	249	29	−108	4.4	2007	9	15	5	26	BUL	0.59
46	36.88	37.84	16	246	55	27	4.4	2007	9	15	11	28	BUL	0.60
47	40.76	39.37	21	229	70	3	4.2	2007	10	27	4	2	BUL	0.64
48	41.10	39.01	18	15	42	−87	4.2	2007	10	28	10	0	BUL	0.53
49	41.25	38.95	14	304	73	159	4.4	2008	6	21	3	58	BUL	0.53
50	37.46	37.71	16	6	41	159	4.2	2008	8	20	11	1	BUL	0.61
51	38.58	37.46	20	226	88	−30	4.8	2008	9	4	10	54	BUL	0.53
52	38.59	37.47	19	224	79	−26	4.4	2008	9	29	8	54	BUL	0.52
53	38.74	38.25	12	340	83	−105	5.0	2009	7	7	3	57	BUL	0.64
54	39.29	38.37	6	250	84	−6	4.0	2009	10	5	1	58	BUL	0.60
55	40.03	38.71	8	329	79	−175	4.3	2010	2	21	4	38	BUL	0.61
56	40.07	38.77	9	202	79	−28	6.0	2010	3	8	2	32	BUL	0.56
57	40.10	38.80	10	20	90	−171	4.4	2010	3	8	3	20	BUL	0.55
58	40.04	38.75	4	315	88	−166	5.3	2010	3	8	7	47	BUL	0.57
59	40.01	38.74	10	136	85	−163	4.2	2010	3	8	8	11	BUL	0.65
60	40.01	38.75	4	156	82	179	4.8	2010	3	8	9	0	BUL	0.64
61	40.05	38.80	6	317	86	−179	4.6	2010	3	8	10	14	BUL	0.61
62	40.03	38.75	7	244	70	0	4.7	2010	3	8	11	12	BUL	0.55
63	40.04	38.74	6	308	79	175	4.4	2010	3	8	2	17	BUL	0.58
64	40.03	38.74	16	308	87	−173	4.8	2010	3	8	3	4	BUL	0.54
65	40.01	38.74	6	54	89	26	4.1	2010	3	9	12	9	BUL	0.65
66	39.99	38.73	16	57	68	−6	4.3	2010	3	9	6	14	BUL	0.55
67	40.14	38.85	18	159	66	−163	4.4	2010	3	9	7	21	BUL	0.64
68	40.04	38.82	14	203	59	14	4.2	2010	3	12	10	50	BUL	0.54
69	40.09	38.77	13	243	41	177	5.0	2010	3	24	2	11	BUL	0.65

Table 1. (continued)

ID	Latitude (deg)	Longitude (deg)	Depth (km)	Strike (deg)	Dip (deg)	Rake (deg)	M	Year	m	d	h	Min	Source[a]	CC Coef
70	39.02	38.11	20	227	89	−1	4.8	2010	9	17	10	17	BUL	0.54
71	39.23	38.46	18	309	89	163	4.1	2011	2	3	3	27	BUL	0.52
72	40.37	39.23	12	32	68	−164	4.4	2011	3	6	7	58	BUL	0.51

[a]BUL, this study; ORG, *Örgülü et al.* [2003]; TAY, *Taymaz et al.* [1991]; MCK, *Jackson and McKenzie* [1988]; INGV, INGV MT catalog; CMT, HARVARD CMT catalog.

velocity model within a broad parameter space (see Figure 4). The final velocity model is selected based on data misfit. The distribution of RMS values shows that the optimized velocity model is well-constrained in terms of the depth of the first velocity discontinuity and the P wave velocities of the first two layers whereas the depth of the crust-mantle boundary (Moho) and the P wave velocity of the uppermost mantle are less well-constrained (Figure 4). Therefore, we fix the crustal thickness based on results from a regional receiver function analysis [*Zor et al.*, 2003]. Using the optimized velocity model for the updated absolute hypocenter location results in significant reduction of travel time residuals. The final hypocenter catalog of the absolute located events consists of 2272 events located with average accuracy better than 5.0 km.

[9] In a second step, we then applied the Double-Difference earthquake relocation method to obtain the highest precision of spatial offset between the earthquake hypocenters [*Waldhauser and Ellsworth*, 2000]. Using relative arrival time data at one station for closely spaced events suppresses the effect of unmodeled velocity structure on hypocentral offsets because the raypaths of paired events are almost identical. Differential travel times can be measured much more precisely than absolute arrival times, resulting in more accurate relative hypocenter locations. We refine manually picked differential travel times using a waveform cross-correlation technique [*Poupinet et al.*, 1984]. The Double-Difference method therefore allows to significantly reduce location errors thereby providing insights into the internal deformation within the EAFZ on a well-resolved scale (Figure 5). The final hypocenter catalog of relocated events consists of 2071 events with an internal accuracy of better than 500 m (Figures 6b and 6d). The accuracy typically ranges between 100 and 200 m which is estimated to be less than or comparable to the size of the source radii of the events. The actual location errors can be even larger than covariance-derived error estimates especially for the event pairs a couple of source sizes away from each other.

[10] For moderate size events we determine moment tensors applying a full-waveform inversion. We analyze 40 events in total covering the magnitude range from M3.9 to M6.0. The inversion approach is based on searching for the tensor parameters giving the best fit between observed and theoretical waveforms. To keep the computation time reasonable, the theoretical waveforms were generated for elementary moment tensors. The parameter space consists of all potential angles for strike, dip and rake (increment 1 degree) as well as the hypocentral depths down to 30 km (increment 1 km). The grid search is performed based on the cross-correlation coefficients giving a measure of the similarity between stimulated and observed waveforms [*Sokos and Zahradnik*, 2008]. The solution providing the highest cross-correlation coefficient is considered to be the best possible solution. Cross-correlation coefficients for the best solutions as a proxy of solution quality are shown in Table 1 (last column). We consider only events with a minimum cross-correlation coefficient of 0.5 at least at 5 stations for further interpretation. This applies only in case of moderate/large size events for which the low frequency content is truly recorded at more than five seismic stations. We add additional events from other moment tensor catalogs available for the target area resulting in a total of 72 mechanisms to elaborate on the kinematics of the entire fault zone over an extended time span (1964–2005 [*McKenzie*, 1972; *Taymaz et al.*, 1991; *Örgülü et al.*, 2003]; INGV and Harvard CMT catalogs).

3. Results

[11] The observed seismicity generally follows the trend of the EAFZ along a ∼20 km wide stripe except for the Celikhan area where off-fault distances of seismicity clusters are larger (Figure 6a). Generally, seismicity is clustered along distinct segments that are sub-parallel to the EAFZ-trend and typically ∼30 km long.

[12] The study area covers the EAFZ segments between Gölbasi (SW) and Bingöl (NE) comprising different tectonic units with various lithological sequences (see Figure 6b). In the Gölbasi – Celikhan – Pütürge area, the fault separates Upper Paleozoic carbonate, clastic rocks and Jurassic-Cretaceous limestones in the northwest from a southeastern nappe region that comprises Paleozoic-Triassic Metamorphites, Upper Cretaceous ophiolites and the volcanic sedimentary Maden Group [*Yilmaz et al.*, 2006]. This area accommodates the seismically least active section of the EAFZ for the time period of our analysis, and has been lastly activated during the 1893 M = 7.1 earthquake [*Ambraseys*, 1971]. Within the observation period most of the seismicity seems to occur on secondary fault structures whereas the main branch of the EAFZ shows only minor seismic activity. Earthquakes occur along the entire seismogenic layer with hypocentral depths extending from 5 to 20 km (Figure 6d). Some secondary fault structures are oriented NW/SE and thus almost normal to the NE-SW oriented main fault (Figure 6b). Focal mechanisms predominantly indicate left-lateral strike slip but also individual thrust and normal faulting events, respectively, that are restricted to local spots of the fault zone (Figure 7). The distribution of faulting mechanisms as well as a relatively low seismic activity observed in the Golbasi-Celikhan-Puturge area suggests that this segment is currently representing a 'seismic gap'. Here the last major (M > 7) event occurred in 1893 indicating that this segment has possibly reached the final phase of the seismic cycle.

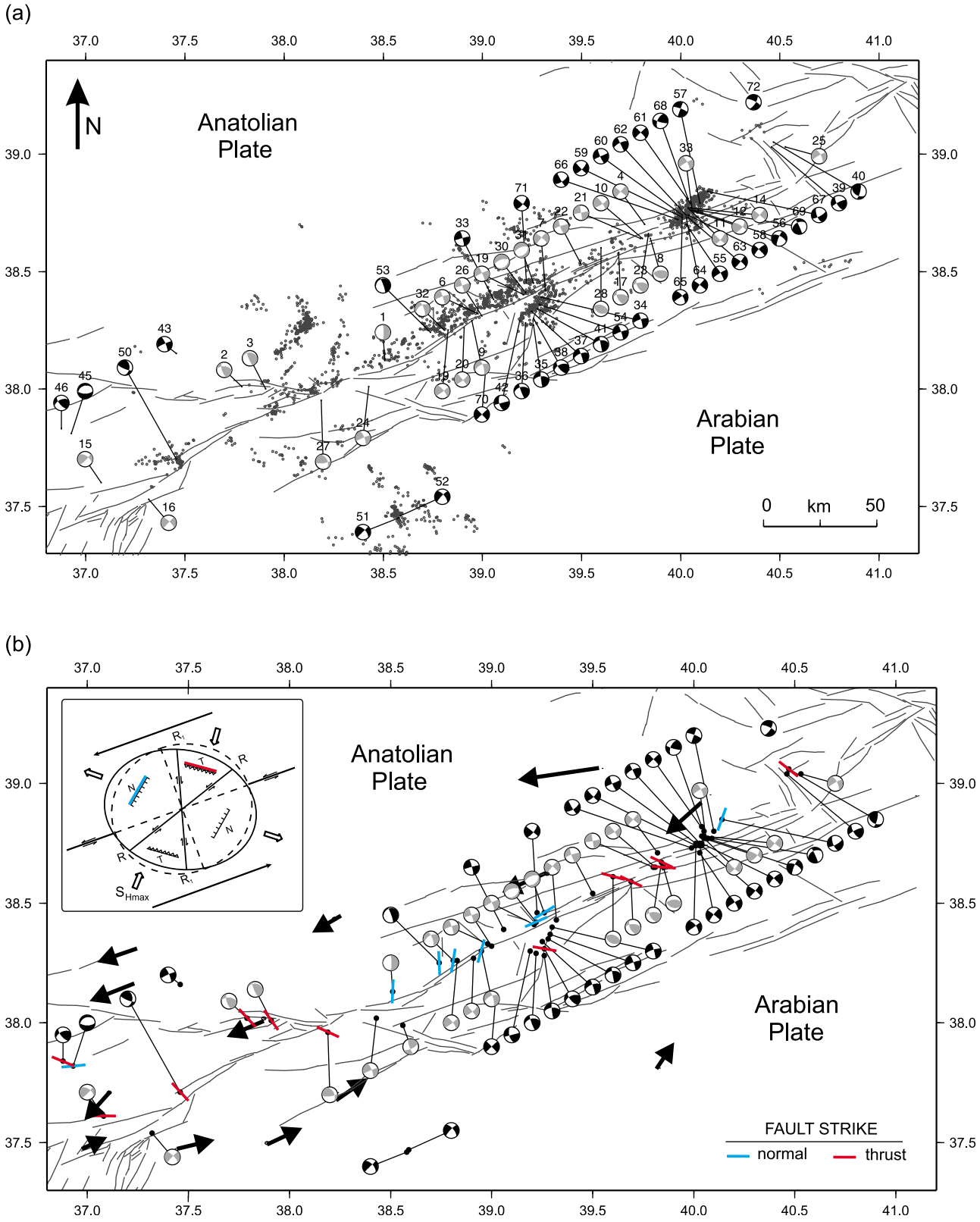
(a)
N
Anatolian Plate
Arabian Plate
0 km 50
37.0
37.5
38.0
38.5
39.0
39.5
40.0
40.5
41.0
(b)
Anatolian Plate
Arabian Plate
FAULT STRIKE
normal
thrust
S Hmax

Figure 7

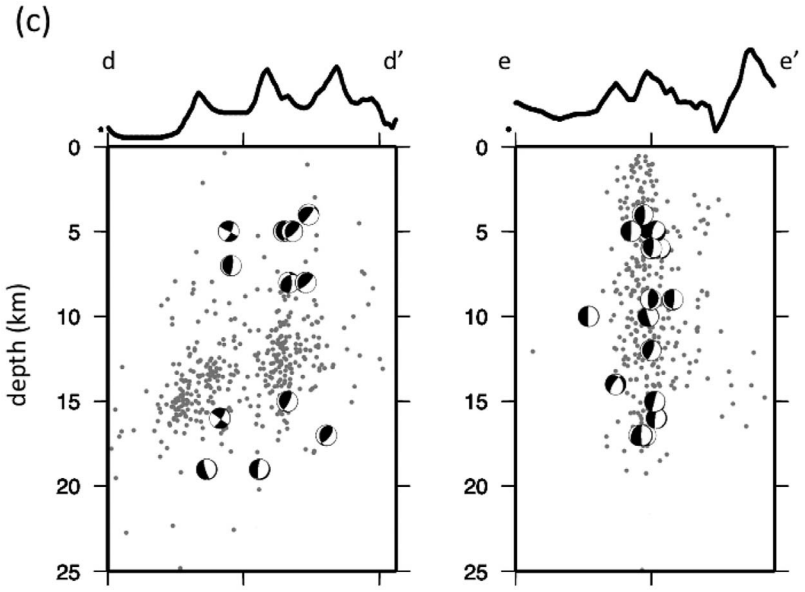

Figure 7. (continued)

[13] The Pütürge-Sivrice-Elazig segments in the central part of the EAFZ are characterized by several basins producing strike-slip faulting, probably along their flanks. The largest basin (Lake Hazar, Figure 6b) is about 5 km wide and 32 km long. Several strike-slip related morphotectonic features are well-exposed in this area [*Aksoy et al.*, 2007]. According to the authors, these features include fault parallel to obliquely orientated pressure and shutter ridges as well as compressional and releasing types of double bends. They include also lensoidal sag-ponds, long and narrow morphologic troughs, S-shaped deflection to offset stream courses, hanging valleys, beheaded streams and fault valleys. The pre-Pliocene basement rocks exposed in the basins consist of Paleozoic-Mesozoic metamorphic rocks, Jurassic-Lower Cretaceous ophilites and the volcanic sedimentary Maden Group [*Aksoy et al.*, 2007]. The basement rocks are overlain by different basin infill (e.g., travertine, stream deposits, fault terrace deposits, fan-delta deposits). These segments currently host the highest seismicity rate throughout the entire study area for the time period of 2007–2010. Due to the high seismicity rate we can image the geometry and spatiotemporal characteristics of these segments in more detail compared to the other sections of the EAFZ. This segment has been lastly activated during the 1875 M6.7 and the 1905 M6.8 earthquakes [*Ambraseys*, 1971]. While the overall distribution of seismicity along the Pütürge/Sivrice segments reflects the regional SW/NE trend of the EAFZ, a prominent structure that splays off the northern part of the Sivrice segment toward the SW is trending ~210° and is thus counter-clockwise inclined with regard to the EAFZ by ~30°. We refer to this splay fault in more detail later in the text. In addition to these larger structures the hypocentral distribution of the relocated events also allows to define smaller but well-constrained fault planes possibly representing NE-SW oriented secondary faults (Riedel shears) and also NW-SE oriented segments (anti-Riedel shears) surrounding the EAFZ (Figure 6b). The hypocentral depth along this part of the EAFZ is concentrated within the depth range of 10–17 km (c-c′ and d-d′ in Figure 6d) while seismicity extends throughout the entire seismogenic zone for most of the other segments (a-a′ and e-e′ in Figure 6d).

[14] The main branch of the EAFZ and the splay fault are the two main active structures in the Sivrice area (Figure 6b). This separation is clearly shown in map view as well as depth distribution based on refined hypocenters (Figures 6b and 6d, profile d-d′). Here the strain accumulation generated by the relative motion of the plates is mainly partitioned to a north-dipping main branch and an almost vertical splay fault.

Figure 7. (a) Combined set of focal mechanisms along the EAFZ for earthquakes analyzed in this study (black beach balls) as well as those published earlier (gray beach balls; 1964–2005 [*McKenzie*, 1972; *Taymaz et al.*, 1991; *Örgülü et al.*, 2003]; INGV and Harvard CMT catalogs). The numbers refer to corresponding information in Table 1. Black dots represent relocated epicenter locations and the gray lines are mapped faults. (b) Local GPS-derived surface displacement field derived from *Reilinger et al.* [2006] and transferred to a EAFZ reference frame (black arrows, see text for details). The inset shows a compilation diagram depicting the structural development of left-lateral strike slip fault during simple shear (R: Riedel shear, R_1: Anti-Riedel shear, N: normal faulting, T: thrust faulting) [*Hancock*, 1985]. Open arrows are the pressure and tension axes, respectively, and black arrows represent the relative motion of the blocks. Focal mechanisms are as in Figure 7a. The fault strikes are represented using red and blue lines corresponding to normal and thrust faulting, respectively (see text for details). (c) Combination of focal mechanisms and relocated hypocenter locations (gray dots) in depth sectional view for two profiles (for profile locations see Figure 6b). Dashed line above shows the corresponding topographic profile that is exaggerated by a factor of two.

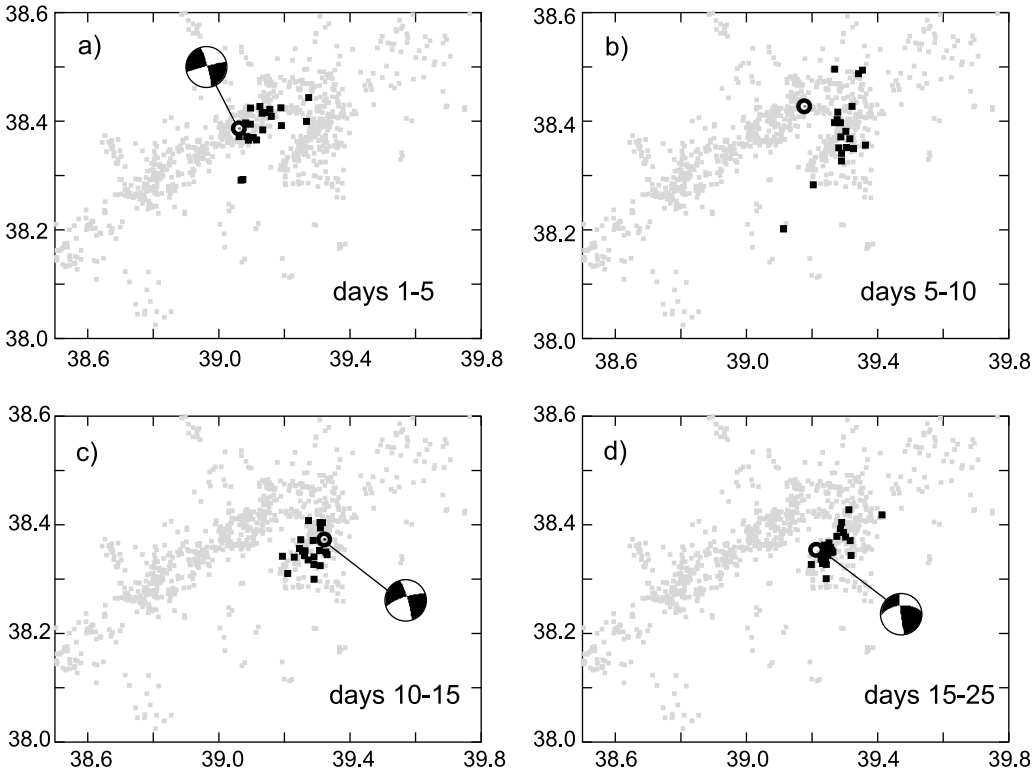

Figure 8. Spatiotemporal evolution of the aftershock seismicity of the 2007 Sivrice earthquakes: Grey dots are the hypocenters located within the entire time period of our analysis for reference. Black dots represent the events for the corresponding time frames as mentioned in lower-right of each subfigure between 09.02.2007–05.03.2007. Open circles are the largest event within each time period and their focal mechanisms, respectively.

While the main branch here accommodates several normal type fault mechanisms, the events along the splay fault are predominantly left-lateral strike slip (Figure 7a). The depth extension of the fault plane imaged by the hypocenter locations roughly correlates with the actual nodal plane of the focal mechanisms (Figure 7c, left). The extension of the fault planes characterized by local hypocenters corresponds to two deep valleys at surface (Figure 7c, top left). The splay fault as mentioned above has been activated by a series of $M > 5$ events in early 2007. Fault mechanisms of these events are in good accordance with the overall left-lateral strike-slip setting of the EAFZ. The largest extensional components in the obtained moment tensors are observed in this area while there are also oblique faults with normal or thrust components, respectively. Precisely relocated earthquake hypocenters of the local seismicity here but especially the aftershocks of the $M > 5$ events provide important hints on the interaction between the main fault and its secondary structures. In the following we particularly focus on the spatiotemporal evolution of a sequence of local seismic activity within a time period of 25 days (09.02.2007–05.03.2007). To further analyze this sequence in space and time we subdivided it in time windows of five or ten days each (Figure 8). The distribution of the events throughout the 25 days shows a remarkable migration of the seismicity starting from the main branch of the EAFZ toward the splay fault. During the first five days a moderate-sized event (M 5.3) has been recorded on 09.02.2007 that occurred right on the main branch triggering aftershock activity in the nearby area around the epicenter (probably reflecting the rupture plane of the main shock) (Figure 8a). During the following five days the activity then migrates toward the splay fault with a few events being located in the initial area and some on the junction from the main fault to the splay fault (Figure 8b). Epicenters of the events during the next five days then exclusively occur on the splay fault completing the migration from main to splay fault with $\sim$10 days (Figure 8c). During the final 10 days activity then remains on the splay fault while individual events again migrate back to the junction.

[15] The Karliova-Bingöl segment of the EAFZ in the northeastern part of our study area is located predominantly in volcanic rocks, mostly Andesite and Basalt [*Arpat and Şaroğlu*, 1972] that cover a sedimentary sequence of Eocene to Miocene. The M = 6.1 2010 Elazığ-Karakoçan earthquake and its aftershock activity is included in our catalog representing the most prominent seismic sequence along the Elazığ – Palu – Bingöl segments of the EAFZ for the time period of our analysis (Figure 6b). Prior to the Elazığ-Karakoçan earthquake this area hosted sparse seismic activity while most events had a dominant thrust-type thrust type fault mechanisms. In contrast, the aftershock sequence consisted mainly of left-lateral strike-slip events mostly occurring on the main branch of the EAFZ. This substantial

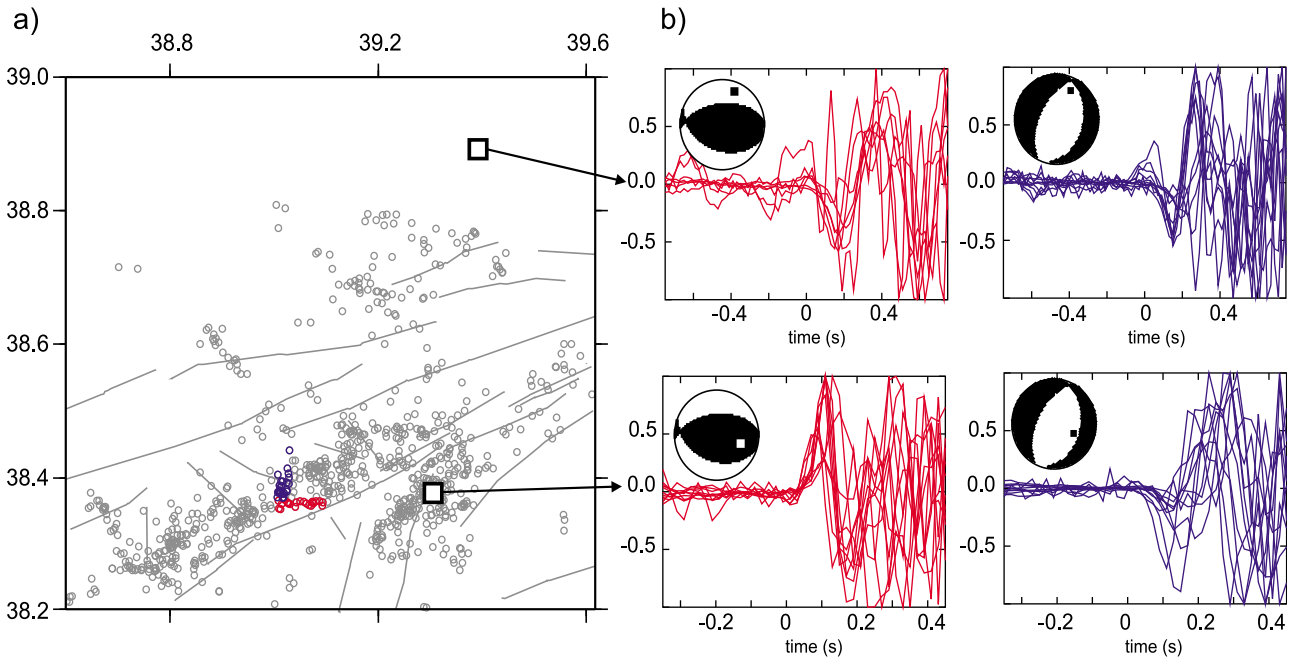

Figure 9. P wave onsets at two selected stations for recordings of earthquakes from two different source areas to elaborate on differentiation of the mechanisms depending on local fault strike: (a) Epicentral map for the Elazığ area based on double-difference locations. Grey circles are the hypocenters for the entire time period of our analysis to refer to the seismically active structures. Red and blue circles are two different seismicity clusters representing EW and NS strikes along the fault zone, respectively. All of these events were too small to reliably determine their focal mechanism. Open squares mark the two closest stations where the first motion data are recorded at reasonable SNR. (b) Observed first motion data and presumable faulting mechanism (inset beach-balls). Squares inside the beach-balls show corresponding points of the respective station on the focal sphere (see text for details). The observed first-motion polarities are consistent with respective focal mechanisms that are in good correlation with the model discussed in the text and shown in Figure 7b.

change in dominant faulting mechanisms may occur at a fault segment during the seismic cycle and initiated by major earthquakes pointing out changes in the local stress field orientation on a particular fault segment [e.g., *Zhao et al.*, 1997; *Hardebeck and Hauksson*, 1999; *Bohnhoff et al.*, 2006]. In that respect it is worth to note that the Elazığ-Karakoçan aftershocks outline a NE-SW oriented epicentral alignment that is slightly inclined counter-clockwise with regard to the overall strike of the EAFZ. A near vertical dip of fault obtained from depth distribution of hypocenters confirms the nodal planes of the focal mechanisms that are predominantly left-lateral strike slip (Figure 7c, right). The fault reflects a well-defined narrow-topographic trace at the surface, which is slightly elevated from the valleys in the Sivrice area (Figure 7c, top right).

4. Discussion

[16] The earthquake catalog presented in this study allows determining the segmentation of the EAFZ and investigating its seismotectonic characteristics based on local to regional seismicity observations for the first time. Spatiotemporal occurrence of seismicity along the fault zone is combined with structural information, faulting mechanisms of the larger events, and the regional GPS-derived velocity field at the surface to characterize deformation behavior of the EAFZ. The improved spatial resolution of seismicity along active fault strands allows better understanding the deformation processes acting on individual EAFZ fault segments and splay faults.

4.1. Segmentation and Fault Zone Characteristics

[17] The observed seismicity follows the overall NE-SW trend of the EAFZ and represents an active band with a width of roughly 20 km. In general, the main branches of the EAFZ form near-vertical planes with pronounced seismic activity between about 5–20 km depth (Figure 6d). This brittle zone is confirmed also by depth range of moment tensor solutions (Figure 7c). Some fault segments are almost aseismic for the time period covered by our observations. In particular, the aseismic section of the fault zone in the SW is surrounded by prominent off-fault seismicity (e.g., 37.5°N/38.5°E and 38.3°N/38.0°E).

[18] In addition to the overall NE-SW trend, the distribution of hypocenters suggests that the EAFZ is also characterized by several smaller ~N-S and E-W oriented subsegments (Figure 6b). In general the southwestern part is seismically less active than the central and northeastern parts. The main fault as defined by its surface trace is surrounded by hypocenters forming near-vertical structures possibly representing fault-parallel oriented segments. In some places, there are also structures oriented sub-parallel to

the main fault trend (e.g., c-c′ in Figure 6b). Fault mechanisms are predominantly left-lateral strike-slip events with one of the nodal planes being (sub-) parallel to the strike of the EAFZ. This is in good agreement with the GPS-derived fault kinematics. In addition, we found several thrust- and normal-faulting events (Figure 7). To extend the observation period we added 33 faulting mechanisms of larger events from the past 50 years as described previously. Analyzing the slip vectors of the five largest earthquakes along the EAFZ since 1960, *Taymaz et al.* [1991] found that the trend of their mean slip vector matches the N60°E direction assumed for the Arabia-Turkey motion as suggested by *Jackson and McKenzie* [1984] and later refined but generally confirmed by GPS measurements [*McClusky et al.*, 2000; *Reilinger et al.*, 2006]. *Taymaz et al.* [1991] also noted a remarkable variety of focal mechanisms along the EAFZ, which is confirmed by our focal mechanism data (see below).

[19] Interestingly, we observe almost no seismicity along the Bitlis-Zagros suture zone (Figure 6) along which the Arabian plate is believed to still converge toward the Anatolian plate [see, e.g., *Flerit et al.*, 2004]. The GPS data also indicates no pronounced convergence at EAFZ-neighboring sections of the Bitlis-Zagros suture zone, which seems currently inactive. This suggests that recently the northward push of the Arabian plate may have slowed down and the EAFZ kinematics possible change from transpression to transtension due to the westward movement of Anatolia that has recently accelerated from 6.5 mm/a (last 13 Ma) to 18–25 mm/a (Holocene and GPS-derived) [*Hubert-Ferrari et al.*, 2002; *Straub et al.*, 1997; *Muller and Aydin*, 2005] caused by the rollback of the Hellenic subduction zone. To further elaborate on local surface deformation along the EAFZ, we transformed the available GPS data [*McClusky et al.*, 2000; *Reilinger et al.*, 2006] into an EAFZ-reference frame by reorienting velocity vectors. The average velocities in E-W and N-S direction for the entire fault zone are subtracted from individual velocity vectors. The resulting vectors represent the displacement field across the fault zone (Figure 7b, black arrows) and indicate a first order strike slip regime with an average trend of 61° +/− 12° i.e., almost parallel to the EAFZ.

[20] In addition to the dominant strike-slip focal mechanisms of the events, we also observe thrust and normal faulting events in all active segments (Figure 7b). Interestingly, the orientations of the nodal planes of these events indicate off-fault subsidiary fault segments, which fit to the overall fault kinematics (Figure 7b, inset). Commonly, N-S oriented fault planes generate normal faulting events (blue lines in Figure 7b) while more E-W oriented planes accommodate thrust faulting events (red lines in Figure 7b). This is in good correspondence with the model earlier proposed by *Hancock* [1985].

[21] We investigate first motion data for the event clusters forming distinct fault planes in order to further elaborate on orientation dependency of fault types. Since the magnitudes of these events are mostly less than M 3.0, the first motion polarities at large distances are not sufficiently visible due to low signal-to-noise ratio (SNR). Therefore we compare the measurements at selected close stations where the SNR is sufficiently large (two stations indicated by open squares in Figure 9a). We selected different event families representing two co-located sub-segments striking E-W and N-S, respectively and superposed all P-onsets at a particular station (red and blue circles, respectively, in Figure 9a). Our observations suggest that the corresponding mechanisms are consistent with thrust and normal faulting, respectively, depending on the trend of the respective hypocenters. At the first station, we observe positive first motion of P waves from events on the E-W striking fault patches (red) and negative first motion of P waves from events on the N-S striking fault patch (blue). The first motions are uniform at both stations for the relevant patch. Projecting the station on the focal sphere of the respective mechanisms is in agreement with the assumed fault mechanisms confirming the conclusion that EW- and NS-trending patches tend to produce thrust faulting and normal faulting, respectively (Figure 9b).

[22] In general, the observed focal mechanisms, the fault pattern, and the velocity field match almost perfectly with kinematic models proposed for the development of strike slip shear zones [e.g., *Tchalenko*, 1970; *Wilcox et al.*, 1973]. Accordingly, NE-SW seismicity alignments that are slightly deviating from the overall strike counter clockwise would represent activity on Riedel shears whereas the almost fault-normal NW-SE oriented hypocenter alignments may represent anti-Riedel shears (Figure 7b, and inset). This observation represents a key example to show evolution of a young shear zone from the kinematic point of view based on seismological data.

4.2. Spatiotemporal Characteristics of Seismicity

[23] The observed seismic activity patterns suggest that neighboring fault segments interact with earthquakes occurring on the main fault possibly triggering seismic events on nearby splay faults (Figure 8). The seismic sequence observed here with hypocenters systematically migrating from an individual fault segment into a splay fault provides important insights in the kinematic interaction between fault segments and their secondary structures and the underlying physical processes raising questions of earthquake triggering (Figure 8). A similar behavior as seen here but at somewhat lower magnitude level (M = 1–2) was also observed at the Princes Islands segment of the North Anatolian Fault Zone below the Sea of Marmara [*Bulut et al.*, 2011]. Although the physical mechanism for the migration of events is still poorly understood, several explanations to it have been previously proposed, e.g., fluid-driven versus tectonically driven stress-triggering [*Chen et al.*, 2012]. We propose that these are likewise potential mechanisms to explain the here observed spatiotemporal distribution. Given the higher magnitudes and larger spatial extension compared to the observation below the Sea of Marmara we note that such phenomena obviously occur on different scales.

[24] To further analyze the development of individual seismicity clusters and the interaction between adjacent clusters in detail we compare the inter-event distance along the fault strike and event origin time along the entire EAFZ (Figure 10). Our hypocenter database covers the time period 2007 to 2011. In order to have a stronger statistical basis, we extend our analysis backward to the year 2003 using the KOERI earthquake catalog (Figure 10a). Comparing both time periods one needs to consider the non-uniform magnitude of completeness (Mc). Therefore we plotted Mc with in Figure 10a (right). This clearly documents that the

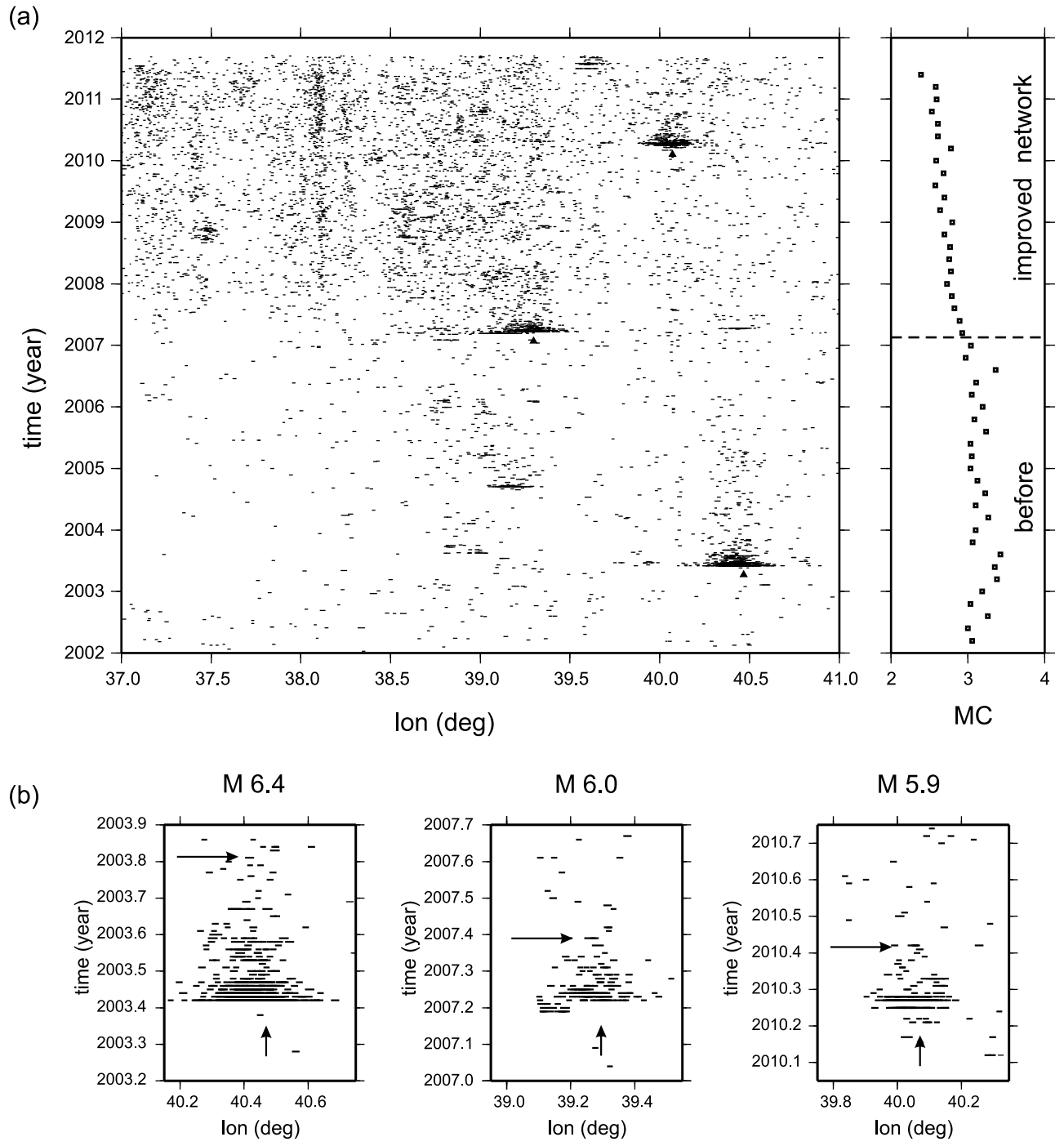

Figure 10. (a) (left) Time-space relations of the seismic activity along the EAFZ. The length of the lines is proportional to the magnitudes of the corresponding events. (right) Variation of the magnitude of completeness with time. Arrows indicate the epicenter of each of the three events, respectively. (b) Enlarged time-space relation plots for the aftershock activities of these events recorded during the time period of our analysis. Lower arrows indicate the main shock location along the fault and the upper arrows indicate the temporal extend of the aftershock activity determined by the Omori-Utsu approach [*Utsu*, 1961].

installation of the seismic network as presented in this study resulted in a substantially lowered Mc after 2007 from M 2.9 to 2.6 on average. However, the main benefit of the intensified network is the higher number of phase arrival times and the ability to obtain well-resolved moment tensors for local events due to improved coverage of the focal sphere.

[25] Several moderate-sized earthquakes (M > 5.0) have been recorded along the EAFZ for the time period 2002–2010. The combined catalog allows characterizing the seismic activity prior to these moderate events. In general, we observe a low rate of seismic activity prior to the M > 5.0 events, which is then increased substantially

during the aftershock periods. This higher activity typically remains for a couple of years (Figure 10a). In particular, this pattern of activity is observed for the 2003 Bingöl, the 2007 Elazığ-Sivrice and 2010 Elazığ-Karakoçan earthquakes (Figure 10b).

[26] The 2003 M = 6.4 Bingöl earthquake activated one of the easternmost conjugates of the EAFZ [*Milkereit et al.*, 2004]. The fault mechanism of the main shock indicates a right-lateral strike-slip likely activating the NW-SE striking Sudüğünü Fault (Figure 6b). The earthquake is preceded by only a few micro-earthquakes recorded during ∼1.5 years before failure which is then followed by enhanced activity for ∼2.5 years (see Figure 10a, at longitude ∼40.5 along the fault strike). Failure then occurred on an adjacent segment toward the west that was activated about seven years later generating a M 6.1 earthquake in Elazığ-Karakoçan area in 2010 (see Figure 10a, at longitude ∼40.5 along the fault strike (see *Tan et al.* [2011] for more information). Note that this time period corresponds to the best available detection threshold for the target area (Figure 10a). This section of the EAFZ follows a similar pattern, which is relatively silent for the pre-seismic period whereas prominent seismic activity is observed for the following 1.5 years. As an example for comparing pre- and post-seismic activity, we note a M = 6.1 event in Elazığ-Sivrice that occurred in Feb 2007. This event is followed by a series of M > 5.0 events (see Figure 10a, between longitudes ∼39.0–39.5 along the fault strike, Figure 10b, left). The earthquake fills one of the seismic gaps along the fault zone, which does not host significant seismicity beforehand.

[27] The temporal evolution of the aftershock activities along the fault zone is well described by the Omori-Utsu law [*Utsu*, 1961]. Here we restrict our analysis to events with magnitudes above 3.0 for which the catalog is assumed to be complete for the entire time period. We consider the aftershock activity to be terminated once the number of events becomes less than 5% of the maximum daily rate (arrows in Figure 10b). Initially, the activity is spread across the entire source region of the main shock. Interestingly, once the activity starts to decay, there seems to be a narrowing of the activity toward the nucleation area of the rupture (lower arrows in Figure 10b). We found this spatiotemporal pattern of aftershock activity for all events with magnitude M > 3.0 recorded during the time period covered by our analysis. We observe that the temporal extend of the aftershock activities scale with the magnitude of the main shock (Figure 10b).

5. Conclusions

[28] We characterize the segmentation and kinematics along the entire East Anatolian Fault Zone (EAFZ) using well-located earthquakes recorded by a dense regional seismic network. Based on relocated hypocenters with a resolution typically ranging between 100 and 200 m, we identify internal deformation of the fault system as well as surrounding splay faults. We find that seismic activity along the EAFZ clusters along distinct ∼30 km long fault segments typically sub-parallel to the overall trend of the fault zone.

[29] Faulting mechanisms are predominantly left-lateral strike-slip and thus in good correlation with the deformation pattern derived from regional GPS data. However, we also observe local clusters of thrust and normal faulting events, respectively. While normal faulting events typically occur on NS-trending subsidiary faults, thrust faulting is restricted to EW-trending structures. This observation is in good accordance with kinematic models proposed for evolving shear zones.

[30] The observed spatiotemporal evolution of hypocenters indicates a systematic migration of micro- and moderate-sized earthquakes from the main fault into adjacent fault segments within several days documenting progressive interaction between the major branch of the EAFZ and its secondary structures.

[31] Analyzing the pre- versus post-seismic phase for M > 5 events we find that aftershock activities are initially spread to the entire source region for several months but start to cluster at the central part of the main shock rupture thereafter.

[32] **Acknowledgments.** The authors wish to thank Helmholtz Foundation for funding the young investigators group from microseismicity to large earthquakes. They gratefully thank Peter Malin, Robert Nowack, Honn Kao, and one anonymous reviewer for constructive comments improving the paper. The seismic network has been partly deployed within the frame of TURDEP project. The authors wish to thank KOERI, TUBITAK, and AFAD for long-term operation of seismic stations.

References

Aksoy, E., M. İnceöz, and A. Koçyiğit (2007), Lake Hazar Basin: A negative flower structure on the East Anatolian Fault System (EAFS), SE Turkey, *Turk. J. Earth Sci.*, *16*, 319–338.

Allen, C. R. (1969), Active faulting in northern Turkey, *Rep. 1577*, 32 pp., Div. of Geol. Sic., Calif. Inst. of Technol., Pasadena.

Ambraseys, N. N. (1971), Value of historical records of earthquakes, *Nature*, *232*, 375–379, doi:10.1038/232375a0.

Ambraseys, N. N., and J. A. Jackson (1998), Faulting associated with historical and recent earthquakes in the Eastern Mediterranean region, *Geophys. J. Int.*, *133*, 390–406, doi:10.1046/j.1365-246X.1998.00508.x.

Arpat, E., and F. Şaroğlu (1972), Some observations and thoughts on the East Anatolian fault, *Bull. Miner. Res. Explor. Inst. Turk.*, *73*, 44–50.

Bird, P. (2003), An updated digital model of plate boundaries, *Geochem. Geophys. Geosyst.*, *4*(3), 1027, doi:10.1029/2001GC000252.

Bohnhoff, M., H. Grosser, and G. Dresen (2006), Strain partitioning and stress rotation at the North Anatolian fault zone from aftershock focal mechanisms of the 1999 Izmit Mw = 7.4 earthquake, *Geophys. J. Int.*, *166*, 373–385, doi:10.1111/j.1365-246X.2006.03027.x.

Bulut, F., W. L. Ellsworth, M. Bohnhoff, M. Aktar, and G. Dresen (2011), Spatiotemporal Earthquake Clusters along the North Anatolian Fault Zone Offshore İstanbul, *Bull. Seismol. Soc. Am.*, *101*(4) 1759–1768, doi:10.1785/0120100215

Çetin, H., H. Güneyli, and L. Mayer (2003), Paleoseismology of the Palu-Lake Hazar segment of the East Anatolian Fault Zone, Turkey, *Tectonophysics*, *374*, 163–197, doi:10.1016/j.tecto.2003.08.003.

Chen, X., P. M. Shearer, and R. E. Abercrombie (2012), Spatial migration of earthquakes within seismic clusters in Southern California: Evidence for fluid diffusion, *J. Geophys. Res.*, *117*, B04301, doi:10.1029/2011JB008973.

Dewey, J. F., and A. M. C. Şengor (1979), Aegean and surrounding regions: Complex multiplate and continuum tectonics in a convergent zone, *Geol. Soc. Am. Bull.*, *90*, 84–92, doi:10.1130/0016-7606(1979)90<84:AASRCM>2.0.CO;2.

Emre, O., and T. Y. Duman (2007), The East Anatolian Fault: Structural pattern and relationship with the Dead Sea Transform, *Eos Trans. AGU*, *88*(52), Fall Meeting Suppl., Abstract T42B-01.

Flerit, F., R. Armijo, G. King, and B. Meyer (2004), The mechanical interaction between the propagating North Anatolian fault and the back-arc extension in the Aegean, *Earth Planet. Sci. Lett.*, *224*, 347–362, doi:10.1016/j.epsl.2004.05.028.

Hancock, P. L. (1985), Brittle micro tectonics: Principles and practice, *J. Struct. Geol.*, *7*, 437–457, doi:10.1016/0191-8141(85)90048-3.

Hardebeck, J. L., and E. Hauksson (1999), Role of fluids in faulting inferred from stress field signatures, *Science*, *285*, 236–239, doi:10.1126/science.285.5425.236.

Hempton, M. R. (1987), Constraints on Arabian plate motion and extensional history of the Red Sea, *Tectonics*, *6*, 687–705.

Hempton, M. R., J. F. Dewey, and F. Şaroğlu (1981), The East Anatolian Transform Fault: Along strike variations in geometry and behaviour, *Eos Trans. AGU*, *62*, 393.

Hubert-Ferrari, A., R. Armijo, G. C. P. King, B. Meyer, and A. Barka (2002), Morphology, displacement and slip rates along the North Anatolian Fault (Turkey), *J. Geophys. Res.*, *107*(B10), 2235, doi:10.1029/2001JB000393.

Jackson, J., and D. P. McKenzie (1984), Active tectonics of the Alpine-Himalayan belt between western Turkey and Pakistan, *Geophys. J. R. Astron. Soc.*, *77*, 185–264.

Jackson, J., and D. P. McKenzie (1988), The relationship between plate motions and seismic moment tensors, and the rates of active deformation in the Mediterranean and Middle East, *Geophys. J. Int.*, *93*, 45–73, doi:10.1111/j.1365-246X.1988.tb01387.x.

Lienert, B. R., and J. Havskov (1995), HYPOCENTER 3.2: A computer program for locating earthquakes locally, regionally and globally, *Seismol. Res. Lett.*, *66*, 26–36, doi:10.1785/gssrl.66.5.26.

McClusky, S., et al. (2000), Global Positioning System constraints on plate kinematics and dynamics in the eastern Mediterranean and Caucasus, *J. Geophys. Res.*, *105*(B3), 5695–5719.

McKenzie, D. P. (1972), Active tectonics of the Mediterranean region, *Geophys. J. R. Astron. Soc.*, *30*, 109–185, doi:10.1111/j.1365-246X.1972.tb02351.x.

McKenzie, D. P. (1978), Active tectonics of the Alpine- Himalayan Belt: The Aegean Sea and surrounding regions, *Geophys. J. R. Astron. Soc.*, *55*, 217–254, doi:10.1111/j.1365-246X.1978.tb04759.x.

Milkereit, C., H. Grosser, R. Wang, H.-U. Wetzel, H. Woith, S. Karakisa, S. Zünbül, and J. Zschau (2004), Implications of the 2003 Bingöl earthquake for the interaction between the North and East Anatolian fault systems, *Bull. Seismol. Soc. Am.*, *94*(6), 2400–2406, doi:10.1785/0120030194.

Muller, J., and A. Aydin (2005), Using geomechanical modeling to constrain the fault geometry within the Marmara Sea, Turkey, *J. Geophys. Res.*, *110*, B03407, doi:10.1029/2004JB003226.

Nalbant, S. S., J. McCloskey, S. Steacy, and A. A. Barka (2002), Stress accumulation and increased seismic risk in eastern Turkey, *Earth Planet. Sci. Lett.*, *195*, 291–298, doi:10.1016/S0012-821X(01)00592-1.

Örgülü, G., M. Aktar, N. Turkelli, E. Sandvol, and M. Barazangi (2003), Contribution to the seismotectonics of Eastern Turkey from moderate and small size events, *Geophys. Res. Lett.*, *30*(24), 8040, doi:10.1029/2003GL018258.

Over, S., S. Ozden, and H. Yilmaz (2004), Late Cenozoic stress evolution along the Karasu Valley, SE Turkey, *Tectonophysics*, *380*, 43–68, doi:10.1016/j.tecto.2003.11.011.

Poupinet, G., W. L. Ellsworth, and J. Frechet (1984), Monitoring velocity variations in the crust using earthquake doublets: An application to the Calaveras Fault, California, *J. Geophys. Res.*, *89*, 5719–5731, doi:10.1029/JB089iB07p05719.

Reilinger, R., et al. (2006), GPS constraints on continental deformation in the Africa-Arabia-Eurasia continental collision zone and implications for the dynamics of plate interactions, *J. Geophys. Res.*, *111*, B05411, doi:10.1029/2005JB004051.

Saroglu, F., O. Emre, and I. Kuscu (1992), *Active Fault Map of Turkey*, Gen. Dir. of Miner. Res. and Explor., Ankara.

Şengör, A. M. C. (1979), The North Anatolian transform fault: Its age, offset and tectonic significance, *J. Geol. Soc.*, *136*, 269–282, doi:10.1144/gsjgs.136.3.0269.

Şengör, A. M. C., and Y. Yilmaz (1981), Tethyan evolution of Turkey: A plate tectonic approach, *Tectonophysics*, *75*, 181–241, doi:10.1016/0040-1951(81)90275-4.

Şengör, A. M. C., et al. (1985), Strike-slip faulting and related basin formation in zones of tectonic escape: Turkey as a case study, in *Strike-Slip Deformation, Basin Formation and Sedimentation*, edited by K. T. Biddle and N. Christie-Blick, *Spec. Publ. Soc. Econ. Paleontol. Mineral.*, *37*, 227–264.

Şengör, A. M. C., O. Tüysüz, C. İmren, M. Sakınç, E. Eyidoğan, N. Görür, X. Le Pichon, and C. Rangin (2005), The North Anatolian Fault: A new look, *Annu. Rev. Earth Planet. Sci.*, *33*, 37–112, doi:10.1146/annurev.earth.32.101802.120415.

Sokos, E., and J. Zahradnik (2008), ISOLA a Fortran code and a Matlab GUI to perform multiple-point source inversion of seismic data, *Comput. Geosci.*, *34*, 967–977, doi:10.1016/j.cageo.2007.07.005.

Straub, C., H.-G. Kahle, and C. Schindler (1997), GPS and geologic estimates of the tectonic activity in the Marmara Sea region, NW Anatolia, *J. Geophys. Res.*, *102*, 27,587–27,601, doi:10.1029/97JB02563.

Tan, O., Z. Pabuçcu, M. C. Tapırdamaz, S. İnan, S. Ergintav, H. Eyidoğan, E. Aksoy, and F. Kuluöztürk (2011), Aftershock study and seismotectonic implications of the 8 March 2010 Kovancılar (Elazığ, Turkey) earthquake (Mw = 6.1), *Geophys. Res. Lett.*, *38*, L11304, doi:10.1029/2011GL047702.

Taymaz, T., H. Eyidoğan, and J. Jackson (1991), Source parameters of large earthquakes in the East Anatolian fault Zone (Turkey), *Geophys. J. Int.*, *106*, 537–550, doi:10.1111/j.1365-246X.1991.tb06328.x.

Tchalenko, J. S. (1970), Similarities between shear zones of different magnitudes, *Geol. Soc. Am. Bull.*, *81*, 1625–1640, doi:10.1130/0016-7606(1970)81[1625:SBSZOD]2.0.CO;2.

Toksöz, M. N., A. F. Shakal, and A. J. Michael (1979), Space-time migration of earthquakes along the North Anatolian fault zone and seismic gaps, *Pure Appl. Geophys.*, *117*, 1258–1270.

Utsu, T. (1961), A statistical study on the occurrence of aftershocks, *Geophysics*, *30*, 521–605.

Waldhauser, F., and W. L. Ellsworth (2000), A double-difference earthquake location algorithm: Method and application to the northern Hayward fault, *Bull. Seismol. Soc. Am.*, *90*, 1353–1368, doi:10.1785/0120000006.

Westaway, R. (1994), Present-day kinematic of the Middle East and eastern Mediterranean, *J. Geophys. Res.*, *99*, 12,071–12,090, doi:10.1029/94JB00335.

Westaway, R. (2004), Kinematic consistency between the Dead Sea Fault Zone and the Neogene and Quaternary left-lateral faulting in SE Turkey, *Tectonophysics*, *391*, 203–237, doi:10.1016/j.tecto.2004.07.014.

Westaway, R., and J. Arger (1996), The Gölbaşı Basin Southern Turkey: A complex discontinuity in a major strike-slip fault zone, *J. Geol. Soc.*, *153*, 729–744, doi:10.1144/gsjgs.153.5.0729.

Wilcox, R. E., T. P. Harding, and D. R. Seely (1973), Basic wrench tectonics, *Am. Assoc. Pet. Geol. Bull.*, *57*, 74–96.

Yilmaz, H., S. Över, and S. Özden (2006), Kinematics of the East Anatolian Fault Zone between Turkoglu (Kahramanmaras) and Celikhan (Adiyaman), eastern Turkey, *Earth Planets Space*, *58*, 1463–1473.

Zhao, D., H. Kanamori, and D. Wiens (1997), State of stress before and after the 1994 Northridge earthquake, *Geophys. Res. Lett.*, *24*(5), 519–522, doi:10.1029/97GL00258.

Zor, E., E. Sandvol, C. Gurbuz, N. Turkelli, D. Seber, and M. Barazangi (2003), The crustal structure of the East Anatolian plateau (Turkey) from receiver functions, *Geophys. Res. Lett.*, *30*(24), 8044, doi:10.1029/2003GL018192.